Geometry and strain effects on single-electron charging in silicon nano-crystals

A. Thean and J. P. Leburton[a)]
Department of Electrical and Computer Engineering, Beckman Institute for Advanced Science and Technology, University of Illinois, Urbana, Illinois 61801

(Received 3 July 2001; accepted for publication 7 September 2001)

We investigate by numerical simulation the effects of geometry and strain on single-electron charging in 100-Å-diameter silicon (Si) nano-crystals of various shapes, embedded in silicon dioxide (SiO_2). Our approach accounts for the Si band structure within the effective mass approximation and a continuum strain model based on the deformation potential theory. Electron–electron interactions in nano-crystals are treated within the density-functional theory. We show that the interplay between the Si nano-crystal geometry and the particular spatial symmetry generated by the strain potential enhances confinement in the quantum-dot and dramatically influences the electronic structure and single-electron charging behavior. In particular, for a Si(001)-oriented truncated-sphere and hemispherical nano-crystals, the 001-oriented orbitals (YY' states) are relatively insensitive to nano-crystal strain compared to orbitals originating from conduction band valleys oriented in the other directions. © *2001 American Institute of Physics.*
[DOI: 10.1063/1.1415543]

I. INTRODUCTION

Efforts to integrate aggressively scaled logic complementary metal–oxide–semiconductor devices and nonvolatile memory for future ultracompact system-on-chip applications are spurring an intensive search for nonvolatile technology with comparable scalability and process requirements as logic devices. Among potential configurations, the nano-crystal (nc) based flash memory is a promising candidate. The first device proposed by IBM[1] utilizes ultrasmall nc's functioning as charge-storage nodes deposited above a thin tunnel oxide, instead of using a single continuous floating gate. These Si-nc's, ranging between 5 and 10 nm in diameters, are essentially quantum dots with strong three-dimensional (3D) quantum-mechanical confinement of carriers, giving rise to pronounced single-electron charging phenomena. Discrete threshold voltage shifts due to single-electron charging in *n*-channel nc memory have been demonstrated at room temperature.[2] While this approach may lead to accurate multibit ultrasmall-size memory devices, the quantum properties of Si-nc's also provide opportunities to investigate low-dimensional physics for potential applications in room-temperature Si quantum systems.

Unlike pattern-defined nanostructures, Si-nc's are usually produced through self-assembling process techniques involving low-pressure chemical vapor deposition and oxidation.[1,3] Hence nc sizes are not limited by lithographic resolution. However, due to inherent variations in growth conditions during self-assembly, variations in nc size, shape, and coverage density are expected. In addition, high resolution transmission electron microscopy and x-ray analysis of nano-crystalline Si in Si/SiO_2 superlattices have revealed an inhomogeneous strain ranging from 0.1% to 3.25%, depending on the nc size and the process annealing temperature.[4] Since single-electron charging and quantum-mechanical carrier tunneling properties are highly sensitive to nc confinement potential, geometry and strain will play important roles in this context. Though single-electron charging in nc memory devices has been theoretically investigated,[5–7] studies of geometry and strain influences on the electronic structure of Si-nc have been scarce,[8,9] if not absent. In this paper, we use a 3D self-consistent computer simulation to study the combined influence of geometry and strain on the electronic structure, and single-electron charging in 100-Å-diameter Si-nc's.

II. MODEL

A single Si-nc embedded in the SiO_2 dielectric between a control gate and a *p*-doped silicon substrate represents the periodic unit-cell of the nc layer in our simulation (Fig. 1). Since the Si-nc's are well-isolated from one another, we assumed that the randomness of their positions in the two-dimensional layer have negligible electrostatic influence among them. Moreover, the fringing fields from the device edges should only affect a limited number of nc's. Hence the use of the periodic boundary condition on the potential for the sides of the unit cell is well-justified.

Our model considers only nc's oriented along the Si[001] direction (Fig. 1) and normal to the Si/SiO_2 tunnel oxide interface, for which electrons occupy only the lowest sixfold-degenerate X valleys. These k-space valleys are labeled according to the orientation of their principal axes, i.e., the two equivalent valleys along the k_x direction are labeled as X-X', and similarly, Y-Y', Z-Z', for the valleys along k_y and k_z, respectively. Though the nc's are likely to be randomly oriented, our choice of the crystal orientation does not limit the generality of our approach towards basic nc physics

a)Electronic mail: leburton@ceg.uiuc.edu

 © 2001 American Institute of Physics

Downloaded 06 Nov 2009 to 129.8.242.67. Redistribution subject to AIP license or copyright; see http://jap.aip.org/jap/copyright.jsp

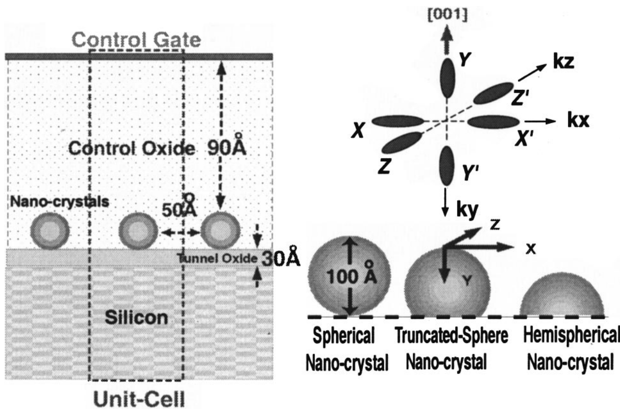

FIG. 1. (left) Schematic of the simulated unit cell of the metal–oxide–semiconductor (MOS) structure with a hemispherical nc-Si embedded in the SiO_2. (right) Schematic of nc shapes and orientations with the six doubly degenerate conduction band valleys considered in our model. The valleys are labeled with respect to the orientation of their principle axis in k space.

of the anisotropic Si band structure. Three different nc prototypical geometries are considered in our analysis, namely spheres, truncated-spheres, and hemispheres [Fig. 1 (right)], which might result from various degrees of wetting during nc nucleation for different growth conditions. We assume that the lateral 100-Å-diameter spherical profile is maintained, while the nc height along the Y direction is varied, and the control oxide and tunnel oxide thicknesses are kept constant. Disorder effects due to lateral geometrical variations are left for future investigations.

The strain in Si/SiO_2 material systems results from the stress buildup caused by molar and thermal expansion during the oxidation of Si into SiO_2, which lead to the bond density mismatch and local strained regions around the interface. Although first-principles atomistic calculations of local strained regions have been performed for planar Si(001)-crystalline SiO_2,[10] an atomistic treatment of nc's is computationally prohibitive due to their complex geometry. However, in our case, because of their relatively large size, the 100-Å-diameter nc's retain their bulk-like behavior. Therefore we choose to investigate the strain arising from the lattice mismatch between Si-nc and SiO_2 within the continuum strain model.[11] We define the relative lattice mismatch between Si and SiO_2 to be $\Delta=(\langle a_{SiO_2}\rangle - a_{Si})/a_{Si}$, where $\langle a_{SiO_2}\rangle$ is the effective lattice constant that represents the isotropic dielectric material and is estimated empirically from strain measurements with planar amorphous SiO_2. The lattice constant for silicon is $a_{Si}=5.431$ Å. With the lattice and bulk elastic constants as parameters, the inhomogeneous strain field is computed at every point according to the continuum strain model by minimizing the elastic energy of the system,[11] which has been described elsewhere.[12] Similar models have successfully studied self-assembled InAs/GaAs pyramidal quantum dots[13,14] and have shown good agreement with atomistic strain calculations for small strain ($\ll 7\%$).[15]

In the deformation potential theory, the strain energy modifies the electronic potential energies which, according to a first-order bulk strain perturbation Hamiltonian,[11,16] gives

$$\Delta E(100)=\Xi_d^{(100)}(\epsilon_{xx}+\epsilon_{yy}+\epsilon_{zz})+\Xi_u^{(100)}\epsilon_{xx}, \tag{1}$$

$$\Delta E(010)=\Xi_d^{(100)}(\epsilon_{xx}+\epsilon_{yy}+\epsilon_{zz})+\Xi_u^{(100)}\epsilon_{zz}, \tag{2}$$

$$\Delta E(001)=\Xi_d^{(100)}(\epsilon_{xx}+\epsilon_{yy}+\epsilon_{zz})+\Xi_u^{(100)}\epsilon_{yy}, \tag{3}$$

where ϵ_{xx}, ϵ_{yy}, and ϵ_{zz} are the position-dependent strain tensor components in the x, y, and z directions, respectively. $\Delta E(100)$, $\Delta E(010)$, and $\Delta E(001)$ are the Si strain energy contributions to the electronic potential energy for the conduction band valleys along the (100), (010), and (001) crystal directions, respectively. $\Xi_u^{(100)}$ and $\Xi_d^{(100)}$ are deformation potentials along the (100) crystal axis with values obtained from Hinckley *et al.*[16] Since the nc electronic wave functions have very limited extent into the SiO_2 barrier, the strain energy in the dielectric region is neglected. The effects of strain on the effective mass are expected to be small since they are a higher order effect[16] and will be left for future investigation. To characterize the nc strain we define the average strain, $\bar{\epsilon}$, by averaging the sum of the hydrostatic strain components over the Si nc region,

$$\bar{\epsilon}=\frac{1}{V}\int_V(\epsilon_{xx}+\epsilon_{yy}+\epsilon_{zz})dxdydz, \tag{4}$$

where V is the nc volume.

In order to gain insights into the nc electronic properties, we compute numerically the quantized electron states $[\psi_l(r)]$ and energy levels (E_l) of the nc by solving three 3D effective-mass Schrödinger-like (Kohn–Sham) equations describing the six triply degenerate conduction band valleys ($l=XX'$, YY', and ZZ'):[5]

$$-\frac{\hbar^2}{2}\nabla[M_l^{-1}\nabla]\psi_l(r)+[-q\phi(r)+(r)+\epsilon_{xc}(n(r)) + \Delta E_l^{\text{strain}}(r)]\psi_l(r)=E_l\psi_l(r). \tag{5}$$

Here M_l is the electron effective mass tensor and $\phi(r)$ is the conduction band landscape of the nc structure, containing the conduction band offset between Si and SiO_2 regions. $\Delta E_l^{\text{strain}}(r)$ is the strain potential relative to the l valley, obtained from Eqs. (1)–(3). The quantum many-body electron–electron interactions in nc's are treated within the density functional theory, with the exchange-correlation potential $\epsilon_{xc}(n)$ computed from the local density approximation (LDA).[17] The numerical iteration algorithm for computing the eigenvectors and eigenvalues is based on the iterative extraction and orthogonalization method technique developed by Jovanovic and Leburton.[18] The boundary conditions for the Kohn–Sham equations are imposed such that the wave functions decay to zero before reaching the device boundaries. The validity of the LDA for small quantum dots, even for one or two electrons, has been demonstrated by Fonseca *et al.* and Shumway *et al.* by using quantum Monte Carlo simulation.[14,19]

The 3D potential, $\phi(r)$, within the device is obtained from the solution of the nonlinear Poisson equation,

$$\nabla[\epsilon(r)\nabla\phi(r)]=-q[p(r)-n(r)-N_A^-(r)], \tag{6}$$

where $n(r)$, $p(r)$, and $N_A^-(r)$ are the electron, hole, and ionized acceptor densities in the Si substrate. $N_A^-(r)$ is cho-

Downloaded 06 Nov 2009 to 129.8.242.67. Redistribution subject to AIP license or copyright; see http://jap.aip.org/jap/copyright.jsp

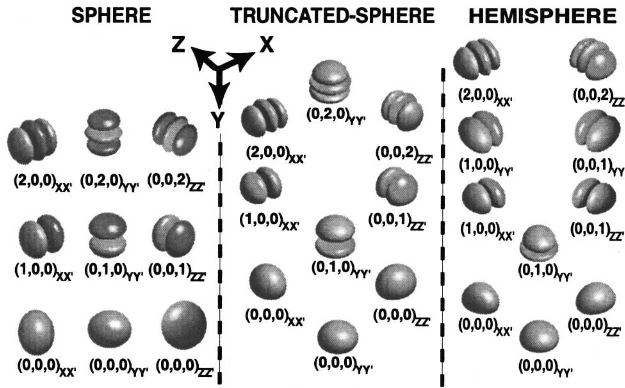

FIG. 2. Orbital ordering in the nc-electronic spectra illustrated by three-dimensional isosurface plots of the first doubly degenerate nine/ten wave functions for 100-Å-diameter spherical nc (left column), 75-Å-high-truncated-sphere nc (middle column), and the hemispherical nc (right column). The energy separation between orbitals are not to scale.

sen to be $1\times10^{17}\,\mathrm{cm}^{-3}$ while other regions of the device structure remain undoped. In the nc, the hole density $p(r)$ is set to zero and the electron density is given by $n(r) = \Sigma_l g_l |\psi_l|^2$, where g_l is the electron state occupation. Otherwise, in bulk silicon, $n(r)$ and $p(r)$ are computed within the Thomas–Fermi approximation. In this analysis we do not resolve individual electron spins. The metallic control gate at the top of the structure is modeled as a Dirichlet boundary condition on the electrostatic potential which varies with gate voltage.[14] The substrate is chosen to be thick enough ($>2\ \mu$m) so that a zero-electric-field (Von-Neumann) boundary condition is imposed at the bottom of the structure.

Single-electron charging is simulated in the low temperature limit ($T=0$ K). This enables us to determine the lowest integer number of electrons, N, in the nc, by using the Slater formula[20,21] which gives directly the difference between the total free energy, E_T, for two electron occupations, N and $N+1$, at each gate bias V_G.

$$E_T(N+1)-E_T(N)=\int_0^1 \epsilon_{\mathrm{LAO}}(n)\,dn \approx \epsilon_{\mathrm{LAO}}(\tfrac{1}{2})-E_F. \tag{7}$$

Here ϵ_{LAO} is the eigenvalue of the lowest available orbital computed from the Kohn–Sham equation occupied by half an electron. E_F is the Fermi energy, which in the present analysis is chosen as the energy reference since the device is at equilibrium. Hence if $\epsilon_{\mathrm{LAO}}(1/2)-E_F$ is positive then $E_T(N+1)-E_T(N)>0$ and the nc contains N electrons, otherwise it contains $N+1$ electrons. Therefore Eq. (7) determines g_l.

III. RESULTS

Figure 2 shows the electronic wave functions for the three nc geometries under the same flat-band condition (no applied electric field). The wave functions are arranged in ascending order of energy according to their electronic spectra, beginning from the ground state at the bottom of each column. The states are labeled in the form $(n_x,n_y,n_z)_i$, where the i index corresponds to the label for the pair of degenerate valleys described by Fig. 1 (right), and the indices (n_x,n_y,n_z) describe the number of nodes of the wave function in the x, y, and z directions, respectively. The spherical nc shows three quadruple-degenerate s-like ground states $[(0,0,0)_{XX'}$, $(0,0,0)_{YY'}$, and $(0,0,0)_{ZZ'}]$ which arise from the symmetry of the spherical confinement and the multivalley band structure. Despite the spherical nc potential, the s wave functions are not spherically symmetric due to the mass anisotropy [Fig. 2 (left)]. Spatially, the wave functions extend more in the direction of the lighter effective mass due to the higher kinetic energy contribution. Similar arguments apply to the (0,0,0)-states from the YY' and ZZ' valleys; they are oriented such that their major and minor axes are always along the direction of lighter and heavier effective masses, respectively. Since electrons tunneling from or into the nc is a strong function of both the quantum-mechanical coupling of the Si channel and the nc wave functions, as well as the effective tunneling cross section, it is worth noticing that the orientation of the degenerate orbitals and their occupations will have a strong influence on the electron transit time across the oxide.

Truncating a 100-Å-diameter sphere by 30 Å in the y direction removes the spherical symmetry of the confinement potential, thereby lifting some of the quantum state degeneracies due to the spherical geometry. Figure 2(middle) shows the wave functions of a nc shaped like a truncated sphere. The (0,0,0) states are no longer at the same energy. The tighter confinement in the y direction now selects the $(0,0,0)_{YY'}$ orbitals, which have the heaviest y-oriented longitudinal effective mass, as the energetically lowest state. The higher $(0,0,0)_{XX'}$ and $(0,0,0)_{ZZ'}$ states remain degenerate because the cylindrical symmetry about the y direction of the nc is preserved. We note that the states in the YY' valleys are not always lower in energy than their counterpart states with the same quantum numbers in the XX' and ZZ' valleys. In Fig. 2(middle), the $(0,2,0)_{YY'}$ states, unlike its parent (0,0,0) and (0,1,0) states, are higher in energy than their counterparts in the other two valleys [i.e., $(2,0,0)_{XX'}$ and $(0,0,2)_{ZZ'}$ states]. This reordering reflects the competition between the heavy longitudinal effective mass along the Y direction, which lowers the energy states, and the increasing influence of the confinement caused by the nc truncation, which lifts the energy states oriented in the same Y direction. These coupled effects of the geometry and the anisotropic band structure can only be captured by a full 3D quantum treatment that accounts for complex geometry.

Further reduction of a truncated-sphere into a hemisphere leads to dramatic changes in the higher energy portion of the electronic spectrum [Fig. 2(right)]. The states with nodes along the lateral directions (x and z directions) now stand lower in the energy spectrum. In fact, we see that the p-like states from the YY'-valleys [i.e., $(1,0,0)_{YY'}$ and $(0,0,1)_{YY'}$], which stand much higher in the spectrum of the truncated sphere, are now less energetic than the (0,0,2)-states in the XX' and ZZ' valleys. This observation illustrates the fact that a slight alteration in nc geometry results in dramatic changes in the nc-electronic structure, which are absent in systems with uniform effective mass like the GaAs/AlGaAs quantum dots.

Downloaded 06 Nov 2009 to 129.8.242.67. Redistribution subject to AIP license or copyright; see http://jap.aip.org/jap/copyright.jsp

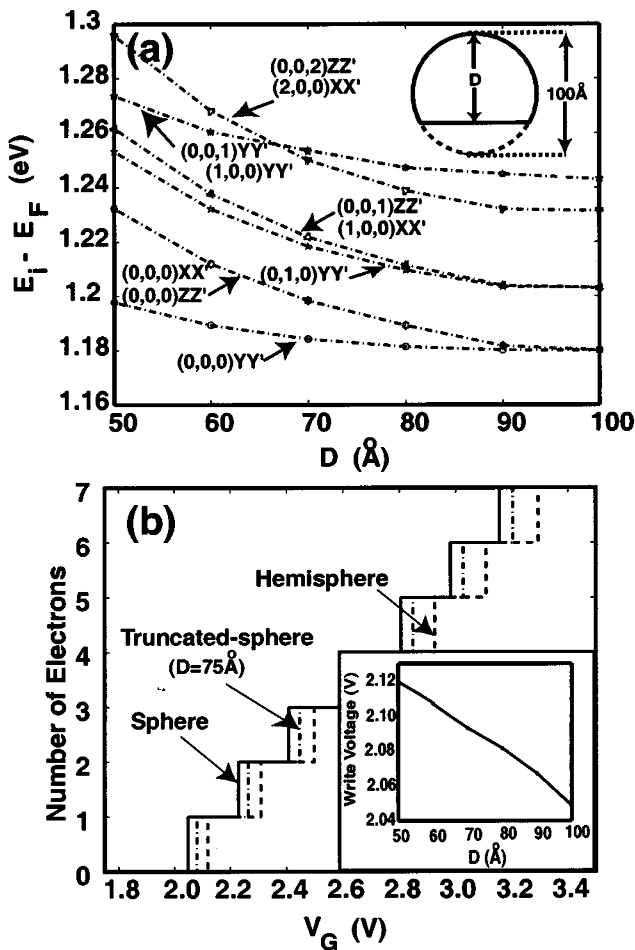

FIG. 3. (a) Electronic energy spectra of an empty nc as a function of nc height D, under flatband condition (zero applied electric field). (b) Coulomb staircase describing single-electron charging for spherical, truncated-sphere, and hemispherical nc. Inset: The write-voltage vs nc height D.

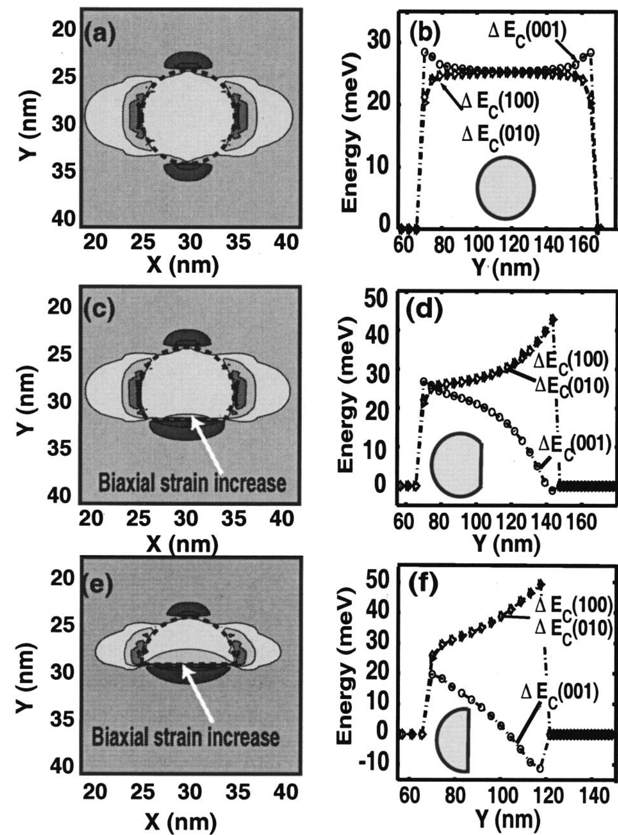

FIG. 4. (a), (c), and (e) are X-Y contour plots of the strain tensor component, ϵ_{xx}, through the center of the spherical, truncated-sphere, and hemispherical nc's, respectively. The plots (b), (d), and (f) are the corresponding line scans (through the nc center) along the Y axis of the Si strain energy.

In Fig. 3(a) we show the variation of the electronic levels with the nc height, D, under flatband condition in the device. As D varies from 50 to 100 Å, the nc shape changes continuously from a hemisphere to a sphere, and all the energy levels decrease, with the electronic states becoming more degenerate. However, the energy-level variations differ greatly from state to state. In particular, the YY' orbitals with no node in the Y direction are much less sensitive to D than the higher states. For instance, the $(0,0,0)_{YY'}$, $(0,0,1)_{YY'}$, and $(1,0,0)_{YY'}$ states only undergo a change of approximately 20 meV, while the other states [including $(0,1,0)_{YY'}$] vary three times or more, when D increases from 50 to 100 Å. We notice that as the height of the nc increases along the Y direction, the single-node $[(0,0,1)_{YY'},(1,0,0)_{YY'}]p$ states, that are orbitals with the heavier y-oriented longitudinal effective mass, move down the spectrum rapidly, crossing the double-node d states $[(0,0,2)_{XX'},(0,0,2)_{ZZ'}]$ in the XX' and ZZ' valleys, at approximately 65 Å [Fig. 3(a)].

Figure 3(b) shows the variations in the single-electron charging behavior of the nc's due to changes in their geometry. We notice the charging voltage for each electron is the smallest for the sphere, and the largest for the hemisphere, while the truncated-sphere is somewhere in between, because of the reduction in the effective confinement volume as the shape varies from a sphere to a hemisphere. In addition, from the step-size difference between the three nc's changes as a function of the electron number, we see the charging voltage variation increases with the electron number. This implies that the write-voltage distribution for a collection of nc's with height variations would have a nonuniform dependence on the charging states as well. If one can exclude the effects of size, lateral shape, and position variations, then the minimum and maximum programming voltages would be bound by that of the sphere and the hemisphere, respectively. The inset of Fig. 3(b) traces the write-voltage variation for charging the nc's with the first electron as a function nc height. The plot shows that the write-voltage decreases by 70 meV as the nc is changed from a 100-Å-diameter hemisphere to a sphere, even though the ground state in an empty nc only experiences less than one-third of this change, as seen in Fig. 3(a). This means that the write-voltage variation cannot be solely explained by the change in the single-particle electronic level, but also includes the subtle quantum and Coulomb many-body effects. Moreover, it is expected that the variation in coupling capacitances between the nc and the rest of the device structure as a consequence of the change in nc shape, would also influence the write-voltage variation.

Next we examine the coupling between geometry and nonuniform strain in the nc's, which introduces new effects on their electronic properties. Figure 4 shows the strain tensor component ϵ_{xx} and the strain potential energies along the

Downloaded 06 Nov 2009 to 129.8.242.67. Redistribution subject to AIP license or copyright; see http://jap.aip.org/jap/copyright.jsp

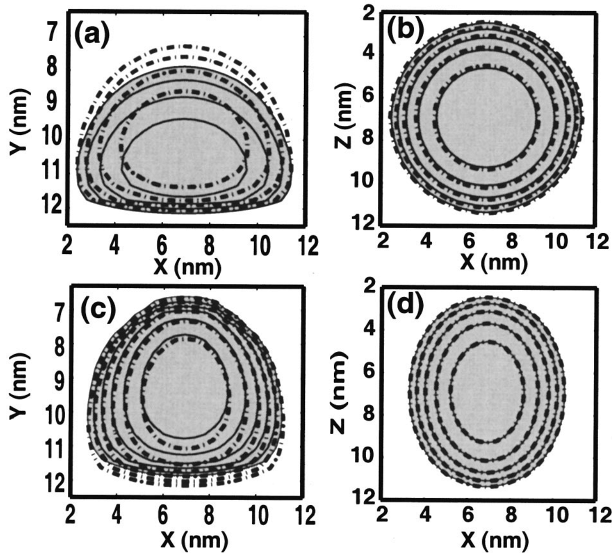

FIG. 5. Contour plots showing the strained (solid-shaded) and unstrained (dashed lines) wave-function amplitudes for (a) and (b) $(0,0,0)_{YY'}$ wave functions and (c) and (d) $(0,0,0)_{XX'}$ wave functions, in the hemispherical nc under an average strain of 3.5%. (The contours are taken from slices through the centers of the nc's.)

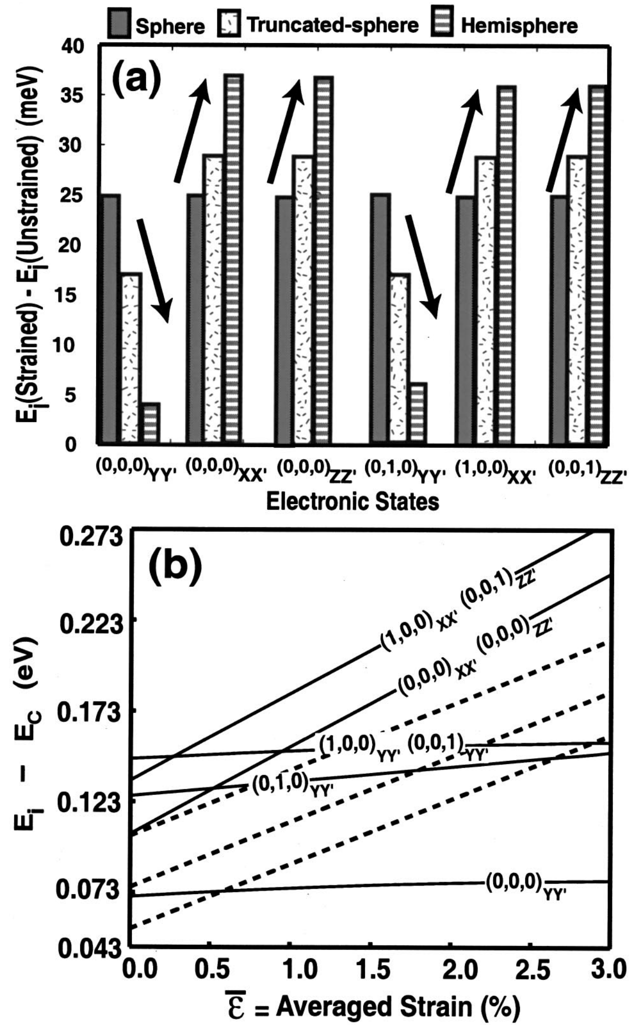

FIG. 6. (a) Effects of strain ($\bar{\epsilon}=3\%$) on the spherical, truncated-sphere ($D=75$ Å), and hemispherical nc's. The arrows illustrate the trend in the strain-induced electronic energy change, as the nc geometry varies from a sphere to a hemisphere. (b) First few energy levels as a function of the averaged strain, $\bar{\epsilon}$, in the hemispherical (solid) and spherical (dashed) nc's. The lowest dash line corresponds to the degenerate (0,0,0) states in the six XX', YY', and ZZ' valleys. The next two higher dash lines refer to the $[(1,0,0_{XX'}),(0,1,0)_{YY'},(0,0,1)_{ZZ'}]$ manifold and the $[(2,0,0)XX', (0,2,0)YY', (0,0,2)ZZ']$ manifold, respectively.

y direction in three nc's with the same 1% lattice mismatch ($\Delta=1\%$). The shape and orientation of the nc's are indicated in the insets. Due to the tension exerted by the SiO_2 on the Si-nc's, the strain energies are largely positive in all three structures. In contrast to the spherically symmetric potential energy variations $\Delta E(001)$, $\Delta E(010)$, and $\Delta E(100)$ of the spherical nc, the truncation leads to an increase in the biaxial tensile strain in the radial X-Z directions ($\epsilon_{xx},\epsilon_{zz}$) and a mildly compressive y component (ϵ_{yy}) at the flat Si/SiO_2 interface causing $\Delta E(100)$ and $\Delta E(010)$ to increase and $\Delta E(001)$ to decrease along y. In Figs. 4(c) and 4(e) we see the development of the ϵ_{xx} biaxial strain increase due to an areal increase of the flat interface as the shape changes from truncated sphere to a hemisphere, which causes a portion of $\Delta E(001)$ to actually turn negative at the flat Si/SiO_2 interface when the truncated sphere is reduced to a hemisphere [Fig. 4(f)]. This change in strain characteristics not only lifts the degeneracy between the YY' valleys and the fourfold degenerate XX'-ZZ' valleys, but also introduces nonuniform strain-enhanced confinement of the electronic states. This is especially evident when we examine the wave functions of the strained hemispherical nc (Fig. 5). In Fig. 5(a) we see that the s-like $(0,0,0)_{YY'}$ wave function corresponding to the strained nc (shaded) is "squeezed" along the Y direction against the flat interface, with respect to the unstrained case (dashed lines). We show that though the strain has increased the confinement vertically along Y, it has little effect radially in the X-Z directions [Fig. 5(b)]. Figure 5(c) and 5(d) show the behavior of the s-like $(0,0,0)_{XX'}$ wave function under the same amount of strain. In this case the strain has shifted the orbital, along Y, towards the top of the nc and the radial profile of the orbital remains hardly affected. This qualitative difference in the strain effects on electronic states from different valleys illustrates the complex interactions between the geometry, strain field, and the band structure.

Figure 6(a) summarizes the effects of strain on the first six orbitals pertaining to three different nc geometries. Each bar on the plot represents the energy difference between the strain and unstrained case, for empty electronic states in nc's and the bars are grouped into three's (sphere, truncated-sphere, and hemisphere) for each orbital designated along the horizontal axis. We see that the strain affects the six orbitals of the spherical nc uniformly. However, the effects experienced by the truncated-sphere and the hemispherical nc's are more subtle. First, an orbital-dependent trend in the energy variation due to strain develops, as one changes the nc shape from sphere to hemisphere. For the states in the YY' valleys, the energy variations tend to increase, changing from sphere to hemisphere, while the XX' and ZZ' states show the opposite trend. This is due to the fact that the YY' states in the hemisphere are much lower energetically than those for the other two shapes, due to the negative dip in strain energy,

Downloaded 06 Nov 2009 to 129.8.242.67. Redistribution subject to AIP license or copyright; see http://jap.aip.org/jap/copyright.jsp

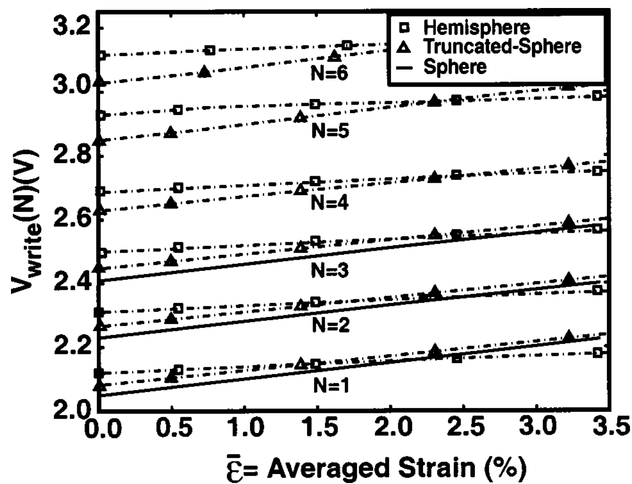

FIG. 7. Write voltages for the first six electrons (only three are shown for the sphere) as a function of average strain for the spherical nc, truncated-sphere ($D=75$ Å), and the hemispherical nc's.

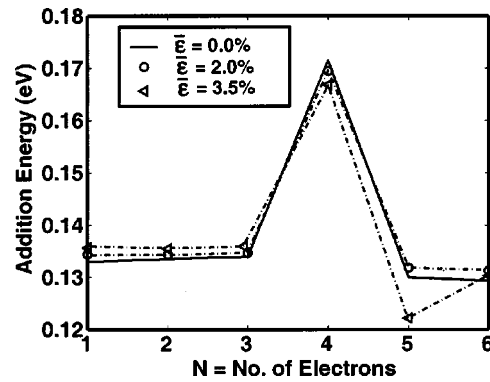

FIG. 8. Addition energy of a hemispherical nc under no strain (solid line), under an average strain of 2% (circles), and under an average strain of 3.5% (squares).

$\Delta E(001)$, at the bottom of the nc [Fig. 4(f)], whereas the XX' and ZZ' states are pushed upward by the strain. We notice in Fig. 6(a) that the strain-induced energy change in the nc-electronic spectrum tend to separate the YY'-states from the XX' and ZZ' states more dramatically in the hemisphere than for the truncated sphere. Qualitatively, this energy separation is a consequence of the increasing strain-induced confinement, as the nc geometry changes from a truncated sphere to a hemisphere, which influences the orbitals in the YY' and the other valleys differently (Fig. 5).

In order to quantitatively investigate the effect of strain on the nc electronic spectrum, we varied the lattice mismatch Δ from 0% to 4% to reproduce the average strain ($\bar{\epsilon}$) measured in Si-nc's. Figure 6(b) compares the effects of strain on the electronic spectrum for the spherical (dash lines) and the hemispherical nc's (solid lines), as a function of average strain, $\bar{\epsilon}$. The eigenenergies are computed with respect to the Si conduction band edge, E_C, which is the bottom of the nc. Again, we observed that the YY' states in the hemispherical nc are much less sensitive to the strain variation than the states in the XX' and ZZ' valleys, varying only 5 meV per 1% change in average strain. We note that this change is also smaller than the 37 meV-per-1%-strain variation experienced by the states in the spherical nc.

Figure 7 shows the strain influence on single-electron charging. The three solid lines correspond to charging the spherical nc with the first three electrons as a function of average nc strain. This corresponds to occupying the $(0,0,0)_{YY'}$ state under different amounts of strain. We see that the write voltage undergoes a 0.15 V increase as the average strain increases from 0% to 3.5%, which is consistent with the monotonic change in the YY' state with strain, discussed in Fig. 6(b). Comparisons between the three nc's show a significant sensitivity of the charging voltage variation to both the nc geometry and strain. We see that the hemispherical nc has the least sensitivity, while the spherical and truncated-sphere nc's are comparable. A feature that stands out from the plot is the write-voltage crossings between the truncated-sphere and hemispherical nc's, which occurs beyond 1.5% strain. These crossings imply that under strain, the energy required to charge a single electron could actually be smaller for the hemispherical nc, despite it being a smaller quantum dot. The locations of these crossings are also dependent on the number of electrons, and they tend to occur at higher strain, when it comes to charging a higher number of electrons.

In Figure 8 we compute the addition energy of the hemispherical nc under an increasing amount of strain as a function of the number of electrons, N, in the nc. The vertical axis represents the energy required to charge the nc from N to $N+1$ electrons. Increasing the amount of strain on the hemispherical nc increases the additional energy for charging the first four electrons ($N=1$ to $N=3$). This variation is approximately 1 meV per 1% increase in average nc strain, and corresponds to charging the $(0,0,0)_{YY'}$ orbitals which are relatively insensitive to strain variations. However, the addition energy for the fifth electron ($N=4$) shows a sudden change, since the most highly strained nc has the lowest peak. This inversion in the addition energy spectra originates from the strain-induced inversion between the $(0,0,0)_{XX'}$ and the $(0,1,0)_{YY'}$ states for $\bar{\epsilon}>0.5\%$ [Fig. 6(b)]. In this case the fifth and higher electrons (up to eight) occupy the $(0,0,0)_{XX'}$ orbitals in the unstrained nc, while the $(0,1,0)_{XX'}$ states are occupied in the strained nc. Moreover, the coupling between the nonuniform strain and the many-body Hartree interactions lead to variations in the addition energy (for $N\geqslant4$) that are strong functions of both N and $\bar{\epsilon}$. We see that in terms of the addition energy spectrum, the nc under a mild 2% strain does not suffer a great change relative to the unstrained case. On the other hand, the behavior of the 3.5%-strained nc shows dramatic changes in its addition energy spectrum, especially for $N=4$ and greater.

IV. CONCLUSION

In summary, our numerical analysis shows that the strain developed between Si and SiO_2 has dramatic influences on the nc electronic states. Specifically, in truncated and hemispherically shaped nc's, the geometry-dependent strain can lift the degeneracy of the Si conduction band valleys and induce greater confinement within the nc's. By varying the magnitude of the strain we show that the electronic spectra

Downloaded 06 Nov 2009 to 129.8.242.67. Redistribution subject to AIP license or copyright; see http://jap.aip.org/jap/copyright.jsp

experience major state reordering in nonspherical nc geometries. We also note that in particular geometries, such as the hemisphere, lower-energy states are quite insensitive to strain effects. This observation suggests the possibility of engineering nc's with strain-immune functional electronic behavior. On the other hand, the control of strain during processing of Si nanostructures will become paramount.

ACKNOWLEDGMENT

This work is partly supported by the NSF Grant No. DESCARTES ECS-98-02730.

[1] S. Tiwari, F. Rana, K. Chan, H. Hanafi, W. Chan, and D. Buchanan, Tech. Dig. - Int. Electron Devices Meet. **1995**, 521.
[2] K. Han, I. Kim, and H. Shin, J. Semicond. Tech. Sci. **1**, 40 (2001).
[3] Y. Shi, K. Saito, H. Ishikuro, and T. Hiramoto, J. Appl. Phys. **84**, 2358 (1998).
[4] M. Zacharias, J. Bläsing, P. Veit, L. Tsybeskov, K. Hirschman, and P. M. Fauchet, Appl. Phys. Lett. **74**, 2614 (1999).
[5] A. Thean and J. P. Leburton, J. Appl. Phys. **89**, 2808 (2001).
[6] A. Thean and J. P. Leburton, IEEE Electron Device Lett. **22**, 148 (2001).
[7] G. Iannaccone and P. Coli, Appl. Phys. Lett. **78**, 2046 (2001).
[8] T-N. Fang and P. P. Ruden, Superlattices Microstruct. **22**, 589 (1997).
[9] A. Thean and J. P. Leburton (unpublished).
[10] A. Pasquarello, M. S. Hybertsen, and R. Car, Appl. Phys. Lett. **68**, 625 (1996).
[11] J. Singh, *Physics of Semiconductors and Their Heterostructures* (McGraw-Hill, New York, 1993).
[12] C. Pryor, M. E. Pistol, and L. Samuelson, Phys. Rev. B **56**, 10404 (1997).
[13] M. Grundmann, O. Stier, and D. Bimberg, Phys. Rev. B **52**, 11 969 (1995).
[14] L. R. C. Fonseca, J. L. Jimenez, J. P. Leburton, and R. Martin, Phys. Rev. B **57**, 4017 (1998).
[15] C. Pryor, J. Kim, L. W. Wang, A. J. Williamson, and A. Zunger, J. Appl. Phys. **83**, 2548 (1998).
[16] J. M. Hickley and J. Singh, Phys. Rev. B **42**, 3546 (1990).
[17] R. G. Parr and W. Yang, *Density-Functional Theory of Atoms and Molecules* (Oxford University, New York, 1989).
[18] D. Jovanovic and J. Leburton, Phys. Rev. B **49**, 7474 (1994).
[19] J. Shumway, L. R. C. Fonseca, J. P. Leburton, R. Martin, and D. Ceperley, Jpn. J. Appl. Phys., Part 1 **38**, 357 (1999).
[20] J. C. Slater, Adv. Quantum Chem. **6**, 1 (1972).
[21] J. F. Janak, Phys. Rev. B **18**, 7165 (1978).

Downloaded 06 Nov 2009 to 129.8.242.67. Redistribution subject to AIP license or copyright; see http://jap.aip.org/jap/copyright.jsp